ASME Journal of Vibration and Acoustics
Online journal at:
https://asmedigitalcollection.asme.org/vibrationacoustics

Nonlinear Energy Transfer of a Spar-Floater System Using the Inerter Pendulum Vibration Absorber

Aakash Gupta
Department of Mechanical Engineering,
Michigan State University,
East Lansing, MI 48824
e-mail: guptaaa3@msu.edu

Van Tuan Kiet Duong
Department of Mechanical Engineering,
Michigan State University,
East Lansing, MI 48824
e-mail: duongkie@msu.edu

Wei-Che Tai[1]
Department of Mechanical Engineering,
Michigan State University,
East Lansing, MI 48824
e-mail: taiweich@msu.edu

The inerter pendulum vibration absorber (IPVA) is integrated between a spar and an annulus floater using a ball-screw mechanism to study its wave energy conversion potential. Hydrodynamic stiffness, added mass, and radiation damping effects on the spar-floater system are characterized using the boundary element method. It is found that a 1:2 internal resonance via a period-doubling bifurcation in the system is responsible for nonlinear energy transfer between the spar-floater system and the pendulum vibration absorber. This nonlinear energy transfer occurs when the primary harmonic solution of the system becomes unstable due to the 1:2 internal resonance phenomenon. The focus of this paper is to analyze this 1:2 internal resonance phenomenon near the first natural frequency of the system. The IPVA system when integrated with the spar-floater system is shown to outperform a linear coupling between the spar and the floater both in terms of the response amplitude operator (RAO) of the spar and one measure of the energy conversion potential of the system. Finally, experiments are performed on the IPVA system integrated with single-degree-of-freedom system (without any hydrodynamic effects) to observe the 1:2 internal resonance phenomenon and the nonlinear energy transfer between the primary mass and the pendulum vibration absorber. It is shown experimentally that the IPVA system outperforms a linear benchmark in terms of vibration suppression due to the energy transfer phenomenon. [DOI: 10.1115/1.4063199]

Keywords: nonlinear vibration, smart materials and structures, vibration control

1 Introduction

Although modern wave energy conversion technology has been studied as early as the 1940s, the oil crisis of 1973 had a major impact on the need for renewable energy. This crisis led to programs on wave energy utilization and its potential to create power by various European nations. Further, in the last few years, research interest in wave energy conversion has increased in North American countries [1]. It is estimated that the annual average wave power incident on the ocean-facing coastlines of North America is over 400 GW (assuming 100% efficiency, which is about 80% electricity consumption for the entire continent [2]). Despite the enormous resources, the cost of using existing wave energy converters (WECs) to generate electricity is higher than solar and wind energy conversion technologies. According to estimates, the levelized cost of energy of wave energy devices (around 570$/MWh) is significantly larger than that of onshore wind or solar photovoltaic energy (≈30$/MWh) [3,4]. Costs of installation, mooring/foundation, operation, and maintenance account for 40–50% of wave energy project life costs [5]. Integration of wave energy converters with already present offshore floating platforms has been shown considerable interest to save the costs of the project [6]. Recently, the oil and gas industry has been investigating the feasibility of converting mature offshore platforms into renewable energy hubs by mounting WECs to the platforms [7]. The WECs can directly supply electricity to the platforms to further lower the cost of wave energy [8].

Offshore floating platforms are worldwide operating in deep water areas for oil and gas production [9] and providing the foundation for floating wind turbines [10]. Specifically, spar platforms establish the buoyancy and stability on a long and slender cylinder that goes deep below the water surface, thereby having good hydrodynamic response/stability and large water depths (600–2500 m for oil spar platforms in the Gulf of Mexico [11]). As the wave energy resources are more abundant in deep water than in shallow water, it is reasonable to integrate WECs and spar platforms. Thus far, several researchers have studied the integration of a spar platform and different types of heaving WECs [12–15]. Heaving WECs refer to a wave energy production system consisting of a floater which primarily moves in heave relative to either a fixed reference (sea bed) or a reacting body (spar, for example) in such a way that the relative heave motion drives a power take-off (PTO) unit for electricity. Existing numerical studies [12,15] suggest that such integration can lead to a 7–30% capture width ratio (hydrodynamic efficiency) of wave

[1]Corresponding author.

Contributed by the Technical Committee on Vibration and Sound of ASME for publication in the Journal of Vibration and Acoustics. Manuscript received March 27, 2023; final manuscript received August 8, 2023; published online September 14, 2023. Assoc. Editor: Guoliang Huang.

energy production, which is comparable with existing heaving WECs [16]. According to the scaling law in Ref. [16], heaving WECs of a larger diameter would have a higher capture width ratio. A typical spar platform in the Gulf of Mexico, e.g., the Horn Mountain, has a diameter of 30 m (Bureau of Safety and Environmental Enforcement data [11]). If the spar-WEC integration in Refs. [12,15] was scaled up to this diameter, the peak mean wave power in operational conditions would be 2.4–10 MW (current floating wind turbines have 5-MW wind power).

Although showing promising results, such integration does not assure good hydrodynamic response of the platform. Past studies have shown that the integration with heaving WECs amplifies the platform heave and pitch motion [12–14], and even causes Mathieu instability [17], which would aggravate fatigue of the mooring and riser systems and even lead to failure of the whole system [18,19]. This deterioration of hydrodynamic response and stability can be explained as follows. Generally speaking, a spar platform has a 20–30 s heave natural period [20,21] which is far away from typical incident wave periods (5–10 s [22]) to avoid large heave resonant response. On the other hand, traditional heaving WECs operate based on the basic principle of linear resonance, thereby having a natural period in heave close to a typical wave period to generate large heave resonant response and hence high-efficiency wave power production [23]. When a heaving WEC is integrated with a platform, this large heave resonant response can give rise to large platform heave/pitch motions. To solve this problem, many solutions have been proposed. Meng et al. [24] used active control in co-located offshore wind-wave systems, where actively altering the wave field with a WEC array by using model predictive control before being incident on a floating offshore wind turbine can result in both motion reduction and reliable energy conversion. On the other hand, there has been a focus on exploiting the internal resonance phenomenon to achieve simultaneous vibration suppression and energy conversion. One such class of systems, known as autoparametric vibration absorbers, due to the existence of an energy transfer phenomenon between a primary system and a pendulum vibration absorber, has been studied for simultaneous vibration suppression and energy conversion [25–28]. This energy transfer phenomenon in autoparametric systems can be achieved using internal resonance [29,30], and thus, systems with internal resonance are getting attention for simultaneous vibration suppression and energy conversion.

Recently, Gupta and Tai performed a pilot study on using an inerter pendulum vibration absorber (IPVA [31]) to extract wave energy from a spar where the IPVA is mounted between the spar and a fixed reference [32]. A major finding is that the IPVA can have resonant responses via 1:2 internal resonance through which the vibration energy of the spar transfers to the pendulum of the IPVA. After integrating with an electromagnetic generator, the IPVA can capture large wave energy production while achieving a good hydrodynamic response of the spar. Motivated by the promising results, this work aims at studying the effect of applying the IPVA to a spar-floater system that is commonly considered as a benchmark model for the integration of the spar and heaving WECs [12,17,14]. As a first attempt, the IPVA system is not integrated with an electromagnetic generator in this work. As such, this work can focus on investigating how the mechanical energy of the spar transfers to the IPVA system through internal resonance without the involvement of electrical energy. In short, the major contributions of this work are two-fold. First, it provides a method to achieve vibration suppression of floating spar platforms when integrated with heaving WECs, which holds the potential to achieve effective wave energy conversion without compromising the platform stability. Second, it presents not only a theoretical analysis but experimental evidences to verify the method.

The remainder of this work is organized as follows. Section 2 talks about the design, analysis, and performance of the IPVA-based spar-floater system. Section 3 discusses the experiments performed on the single-degree-of-freedom "dry" IPVA system, with focus on nonlinear energy transfer between the primary system and the pendulum vibration absorber. Finally, Sec. 4 summarizes the main findings and concludes this study.

2 IPVA-Based Spar-Floater System

This section describes the design, analysis, and performance of the IPVA-based spar-floater system.

2.1 Design of the System. Figure 1(*a*) shows a spar and an annular floater floating in water. For simplicity, the spar and floater are constrained such that they can only move in the heaving (x) direction relative to the waterline. Figure 1(*b*) shows the IPVA system consisting of a lead screw, a carrier, and a pendulum vibration absorber. The nut of the lead screw is fixed to the floater while the screw is supported by a thrust bearing that is fixed to the spar through a housing. As a result, the relative heaving displacement $x_1 - x_2$ is converted into the angular displacement θ through $x_1 - x_2 = R\theta$, where $R = L/2\pi$, and L is the screw lead. The carrier is fixed to the screw such that they have the same angular displacement (θ). The pendulum pivots on a point of the carrier which is located at a distance of R_p from the carrier center. The pendulum has length r and an angular displacement ϕ with respect to the screw. Figure 1(*c*) shows the mathematical model of the system where k_1 and k_2 denote the hydrostatic stiffness in heave of the spar and the floater, respectively, and M_1 and M_2 denote the mass of the spar and the floater, respectively. Furthermore,

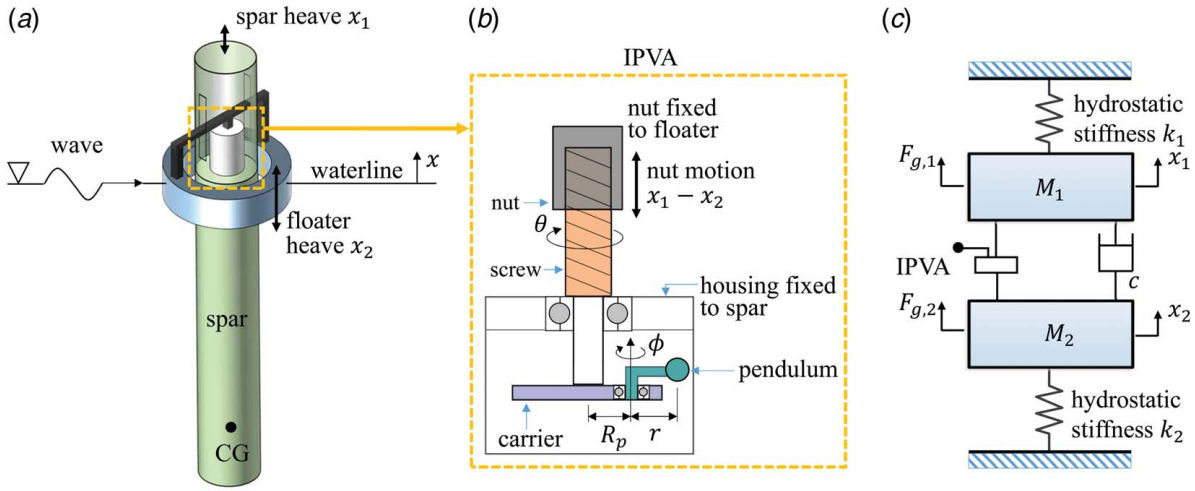

Fig. 1 Ocean wave energy harvesting design

Fig. 2 ANSYS AQWA model for calculation of hydrodynamic coefficients

the wave motion generates hydrodynamic forces $F_{g,1}$ and $F_{g,2}$, exciting the spar and the floater, respectively. Linear wave theory is assumed for the current analysis, and the derivation of the hydrodynamic coefficients on the system, along with the equation of motion is discussed in the next section.

2.2 Equations of Motion. To facilitate deriving the equations of motion, the following coordinate transformation is employed:

$$x_2 = R\psi$$
$$x_1 = R(\theta + \psi) \tag{1}$$

Euler–Lagrange mechanics is used to derive the equations of motion. The kinetic and potential energy of the system are determined, followed by the hydrodynamic coefficients of the system. Finally, the virtual work due to the forces applied to the system is derived and the equations of motion are normalized.

First, the sum of the kinetic energy of the spar, floater, and the IPVA system, and the sum of the potential energy of the spar and floater are given by

$$T = \frac{1}{2}J_p(\dot{\theta}+\dot{\phi})^2 + \frac{1}{2}J_{bsc}\dot{\theta}^2 + \frac{1}{2}m\left[\dot{\theta}^2\left(r^2 + 2rR_p\cos\phi + R_p^2\right)\right.$$
$$\left. + r^2\dot{\phi}^2 + 2r\dot{\theta}\dot{\phi}(r + R_p\cos\phi)\right] + \frac{1}{2}M_1(R\dot{\theta}+R\dot{\psi})^2 + \frac{1}{2}M_2R^2\dot{\psi}^2$$
$$V = \frac{1}{2}k_1(R\theta + R\psi)^2 + \frac{1}{2}k_2R^2\psi^2 \tag{2}$$

where T and V are kinetic and potential energy respectively. Here J_{bsc} and J_p are the moments of inertia of the ball-screw-carrier assembly and of the pendulum respectively. Further, m denotes the mass of the pendulum. Next, the hydrodynamic coefficients of

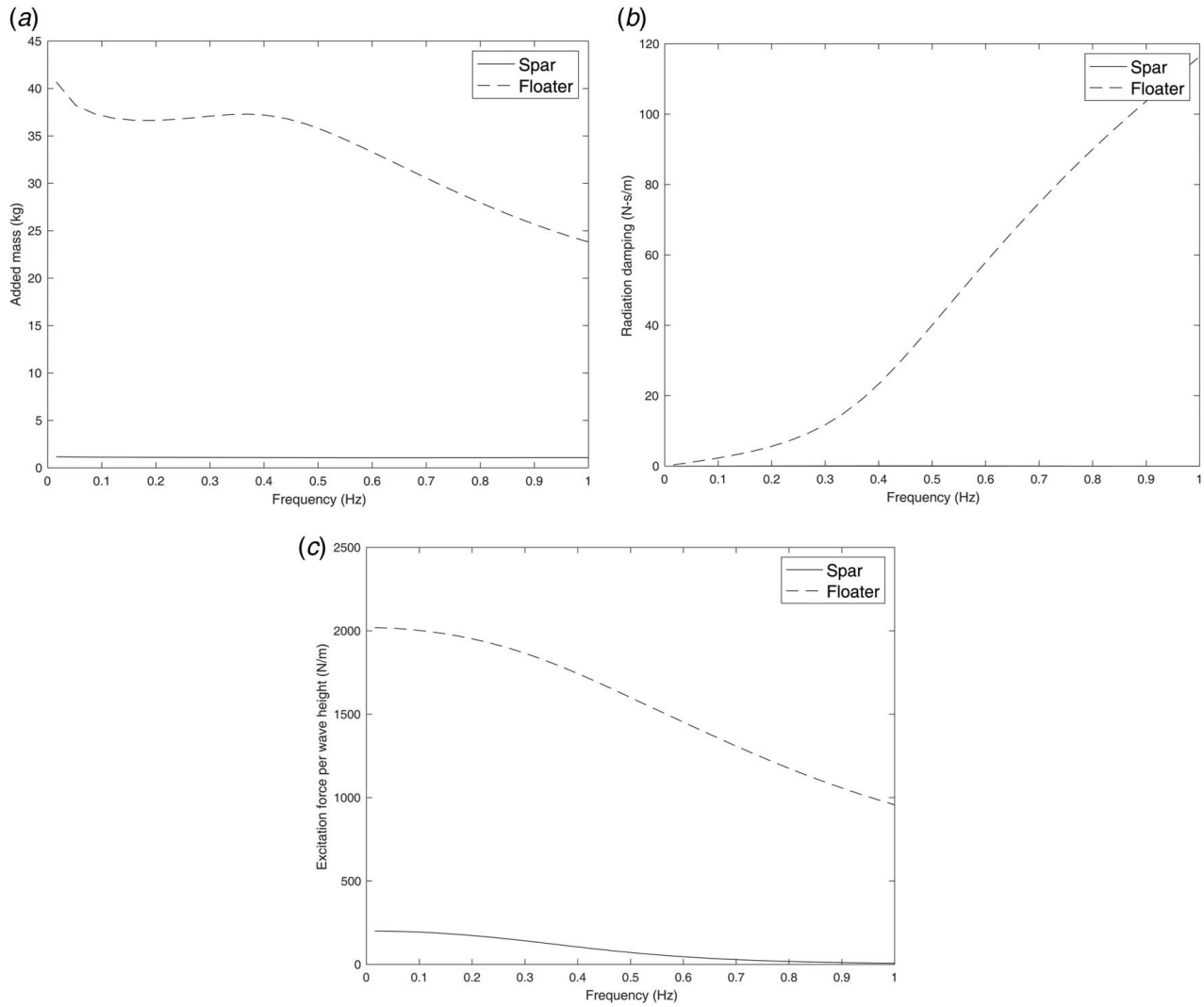

Fig. 3 (*a*) Added mass, (*b*) radiation damping, and (*c*) diffraction and Froude–Krylov forces for spar and floater

the spar and the floater subject to incident regular waves are determined by the linear wave theory, which assumes that the fluid is inviscid and irrotational [33]. Based on the linear wave theory, the hydrodynamic force on the spar and the floater consists of three components: Froude–Krylov force, diffraction force, and radiation force. The first term corresponds to the undisturbed incident wave field without the present of spar-floater system, whereas the diffracted force is the result of modification in the incident wave field due to presence of the spar-floater system, and the radiation force results from the oscillations in the spar-floater system.

The Froude–Krylov and diffraction forces together give rise to the excitation force while the radiation force gives rise to the added mass and radiation damping [22,33], which can be represented by the well-known Cummins' equation [34]

$$F_{g,i} = -A_{\infty,i}\ddot{x}_i - \int_{\sigma=0}^{\infty} k_{R,i}(\sigma)\dot{x}_i(t-\sigma)\mathrm{d}\sigma + \gamma F_i(t), \quad i = 1, 2 \tag{3}$$

where γ is the wave amplitude, $F_{g,i}$ is the incoming wave force, $f_i = \gamma F_i$ is the excitation (Froude–Krylov and diffraction) force, and F_i is the excitation force per wave amplitude. Here $F_{g,i}$, and as a consequence F_i, are assumed to be sinusoidal with angular frequency Ω equal to the angular frequency of the incoming wave. The radiation impulse response kernel, $k_{R,i}(\sigma)$ and the radiation infinite-frequency added mass, $A_{\infty,i}$, are related to the radiation frequency-dependent damping and added mass $B_{R,i}(\Omega)$ and $A_{R,i}(\Omega)$, through Ogilvie's relations [35]

$$\begin{aligned} B_{R,i}(\Omega) &= \int_{\sigma=0}^{\infty} k_{R,i}(\sigma)\cos(\Omega\sigma)\mathrm{d}\sigma, \quad i = 1, 2 \\ A_{R,i}(\Omega) &= A_{\infty,i} - \frac{1}{\Omega}\int_{\sigma=0}^{\infty} k_{R,i}(\sigma)\sin(\Omega\sigma)\mathrm{d}\sigma, \quad i = 1, 2 \end{aligned} \tag{4}$$

and

$$A_{\infty,i} = \lim_{\Omega\to\infty} A_{R,i}(\Omega) \tag{5}$$

The hydrodynamic coefficients $A_{R,i}(\Omega)$ and $B_{R,i}(\Omega)$, Froude–Krylov and diffraction forces $f_i(t)$ are determined using ANSYS AQWA. For the calculation of the hydrodynamic coefficients, the spar-floater system was modeled together but was not coupled physically, though they influenced each other's hydrodynamics. A convergence test was performed like previously illustrated in Ref. [32] to match the published results in Ref. [36]. After verifying the ANSYS model, the same setting is adopted to simulate the spar-floater system for the rest of the paper. The height of the spar is taken as 1.06 m with a draft of 0.96 m (the height of the spar below the surface of the water), and a diameter of 0.16 m, which is the 1:100 reduced sparD model with water depth of 3 m described in Ref. [37]. The floater, on the other hand, is an annulus with a depth of 0.02 m with inner diameter of 0.317 m and outer diameter of 0.595 m. Figure 2 shows the mesh of the system used for analysis and Fig. 3 shows the added mass, radiation damping, and excitation force obtained using ANSYS for both the spar and the floater. Table 1 shows the physical properties of both the spar-floater system (obtained via ANSYS AQWA) and the ball-screw transmission chosen for this study. All the data in SI units.

Next, let's look at the virtual work due to various forces on the system. The total virtual work in the system is

$$\delta W = \delta W_{AM} + \delta W_{RD} + \delta W_F + \delta W_D \tag{6}$$

where δW_{AM}, δW_{RD}, δW_F, and δW_D are the virtual works due to the added mass, radiation damping, excitation force, and mechanical damping, respectively, and are calculated as follows:

$$\begin{aligned} \delta W_{AM} &= -A_{\infty,1}\left(\ddot{\theta} + \ddot{\psi}\right)R^2\left(\delta\theta + \delta\psi\right) - A_{\infty,2}R^2\ddot{\psi}\delta\psi \\ \delta W_{RD} &= -\left[\int_0^{\infty} R^2\kappa_1(\sigma)\left(\dot{\theta}(t-\sigma) + \dot{\psi}(t-\sigma)\right)\mathrm{d}\sigma\right]\left(\delta\theta + \delta\psi\right) \\ &\quad - \left[\int_0^{\infty} R^2\kappa_2(\sigma)\dot{\psi}(t-\sigma)\mathrm{d}\sigma\right]\delta\psi \\ \delta W_F &= Rf_1\left(\delta\theta + \delta\psi\right) + Rf_2\delta\psi \\ \delta W_D &= -cR^2\dot{\theta}\delta\theta - c_p\dot{\phi}\delta\phi \end{aligned} \tag{7}$$

Using these equations, the θ, ϕ, and ψ contributions due to virtual work into the equations of motion can be obtained. After substituting the kinetic and potential energy and the virtual work, and using the following normalization parameters:

$$\begin{aligned} &\eta_g = \frac{J_r}{M_1R^2}, \quad \mu_F = \frac{M_1}{M_2}, \quad \eta = \frac{r}{R_p}, \quad \omega_0 = \sqrt{\frac{k_1}{M_1}}, \quad \omega_2 = \sqrt{\frac{k_2}{M_2}}, \\ &\mu_r = \frac{mR_p^2}{M_1R^2}, \quad \omega = \frac{\Omega}{\omega_0}, \quad \omega_r = \frac{\omega_2}{\omega_0}, \quad \tau = \omega_0 t, \\ &\xi = \frac{c}{2\omega_0 M_1}, \quad \xi_p = \frac{c_p}{2\omega_0 M_1R^2}, \quad ()' = \frac{\mathrm{d}()}{\mathrm{d}\tau}, \quad f_{e,1} = \frac{f_1}{\omega_0^2 M_1 R}, \\ &f_{e,2} = \frac{f_2}{\omega_0^2 M_1 R}, \quad \mu_{A\infty,1} = \frac{A_{\infty,1}}{M_1}, \quad \mu_{A\infty,2} = \frac{A_{\infty,2}}{M_1} \end{aligned} \tag{8}$$

the following equations of motion are obtained:

$$\mathbf{M}\mathbf{x}'' + \mathbf{C}\mathbf{x}' + \mathbf{K}\mathbf{x} + \mathcal{R}(\mathbf{x}') = \mathbf{F} \tag{9}$$

where

$$\mathbf{M} = \begin{pmatrix} \eta^2\mu_r + \mu_{bsc} + \mu_r + \mu_p + 2\eta\mu_r\cos\phi + 1 + \mu_{A\infty,1} & 1 + \mu_{A\infty,1} & \mu_p + \eta^2\mu_r + \eta\mu_r\cos\phi \\ 1 + \mu_{A\infty,1} & \mu_F + 1 + \mu_{A\infty,1} + \mu_{A\infty,2} & 0 \\ \mu_p + \eta^2\mu_r + \eta\mu_r\cos\phi & 0 & \mu_p + \eta^2\mu_r \end{pmatrix}$$

$$\mathbf{C} = \begin{pmatrix} 2\xi & 0 & 0 \\ 0 & 0 & 0 \\ 0 & 0 & 2\xi_p \end{pmatrix}, \quad \mathbf{K} = \begin{pmatrix} 1 & 1 & 0 \\ 1 & 1 + \mu_F\omega_r^2 & 0 \\ 0 & 0 & 0 \end{pmatrix}$$

$$\mathbf{F} = \begin{pmatrix} f_{e,1} + 2\eta\mu_r\theta'\phi'\sin\phi + \eta\mu_r\phi'^2\sin\phi \\ f_{e,1} + f_{e,2} \\ -\eta\mu_r\theta'^2\sin\phi \end{pmatrix}$$

$$\mathcal{R} = \frac{1}{M_1\omega_0^2}\begin{pmatrix} \int_0^{\infty}\kappa_1\left(\frac{s}{\omega_0}\right)\left[\theta'(\tau-s) + \psi'(\tau-s)\right]ds \\ \int_0^{\infty}\kappa_1\left(\frac{s}{\omega_0}\right)\left[\theta'(\tau-s) + \psi'(\tau-s)\right]ds + \int_0^{\infty}\kappa_2\left(\frac{s}{\omega_0}\right)\psi'(\tau-s)ds \\ 0 \end{pmatrix}, \quad \mathbf{x} = \begin{pmatrix} \theta \\ \psi \\ \phi \end{pmatrix}$$

Table 1 Parameters for spar-floater system

Parameter	Value
M_1	19.46
M_2	4.08
k_1	198.79
k_2	2001.04
R	0.0672
$A_{\infty,1}$	1.078
$A_{\infty,2}$	12.418

Note: All the data in SI units.

2.3 Period-Doubling Bifurcation in the IPVA System. Following the idea laid out in the previous work by the authors [31,32], the boundary of parametric instability where the primary harmonic solution of the system becomes unstable can be obtained. To that end, the harmonic balance analysis with the modified alternating frequency time (AFT) method and Floquet theory are used as elaborated in Ref. [32].

As has been reported previously in Refs. [31,32], the instability in the primary solutions for the system due to period-doubling bifurcations gives rise to additional terms in the ball screw (θ) and pendulum's response (ϕ), referred to as secondary solutions (with harmonics of frequency $\frac{\omega}{2}$ where ω denotes the wave excitation frequency) in the system. This period-doubling bifurcation gives rise to 1:2 internal resonance in the system. We use the bifurcation tracking algorithm developed in Ref. [31] with modified AFT method proposed in Ref. [32] to obtain the period-doubling bifurcation boundary. The boundary in Fig. 4 shows the wave height on the y-axis and wave frequency on the x-axis. Like the results in Refs. [31,32], below this boundary, the primary harmonic solution is stable and above this boundary, the period of the solution doubles. To verify this behavior, the hydrodynamic response with three wave heights (× 1, ×2, and ×3, ×3 not shown), corresponding to 4.5 cm, 5.4 cm, and 12 cm at a frequency of 0.44 Hz, is simulated by using the explicit Runge–Kutta (4,5) integration method. The integration kernel is evaluated using an impulse to state-space converter function described in Refs. [32,38]. Figures 5, 6, and 7 show the response of the pendulum (ϕ) and the fast Fourier transform (FFT) of the response of the pendulum, and the ball-screw system (θ). Note that $\hat{\omega}$ represents the frequency of oscillation normalized with respect to the wave frequency, which means that $\hat{\omega}$=1 corresponds to the primary component of the solution, and $\hat{\omega} = \frac{1}{2}$ represents oscillation of angular frequency $\frac{\omega}{2}$, ω being the wave excitation frequency. As can be observed from these figures,

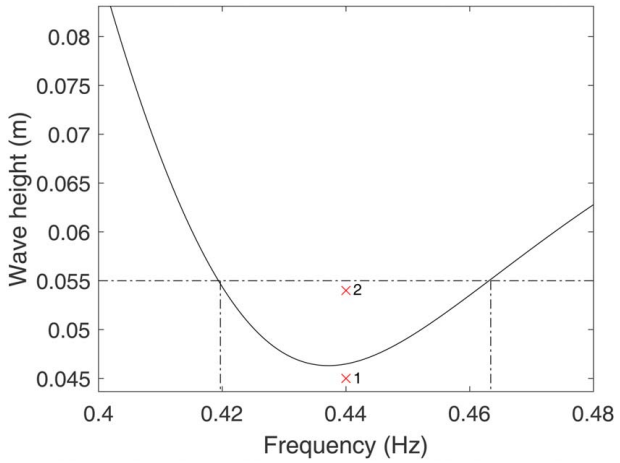

Fig. 4 Stability boundary for the primary harmonics of the system for $\mu_r = 0.2$, $\eta = 0.3$, $\xi = 0.05$, $\xi_p = 0.02$, $\mu_p = 0.039$, $\mu_{bsc} = 0.1$

below the stability boundary the solution is strictly primary, whereas at point ×2, the motion of the pendulum (along with the ball screw) contains harmonics of frequency $\frac{\omega}{2}$, in addition to the primary harmonics. If we further increase the wave height to point ×3, the time series of the pendulum's motion shows intermittent rotation and oscillation, whereas the FFT shows the motion of the pendulum (and the ball screw) consisting of many frequencies, showing non-periodic behavior. This observation has been recorded previously by the authors in Ref. [31], and the response can be attributed to a cascade of period-doubling bifurcation which eventually can lead to chaotic-like motions in the system, as evident from response at point 3. It has been noted previously in this work that the crossing of the period-doubling bifurcation boundary results in energy transfer between the primary (spar-floater) system and the pendulum vibration absorber. To demonstrate this, we fix a wave height, say 5.5 cm (which is above the instability boundary for a frequency range from approximately 0.42–0.465 Hz, as marked by vertical dashed lines in Fig. 4), and look at the frequency response of the proposed system.

2.4 Nonlinear Energy Transfer and Energy Harvesting Potential. As mentioned in the previous section, for the wave height of 5.5 cm, we expect an energy transfer between the spar-floater system and the pendulum for the specified frequency range. To benchmark this system, we use a linear system defined as the system with the pendulum locked such that its first natural

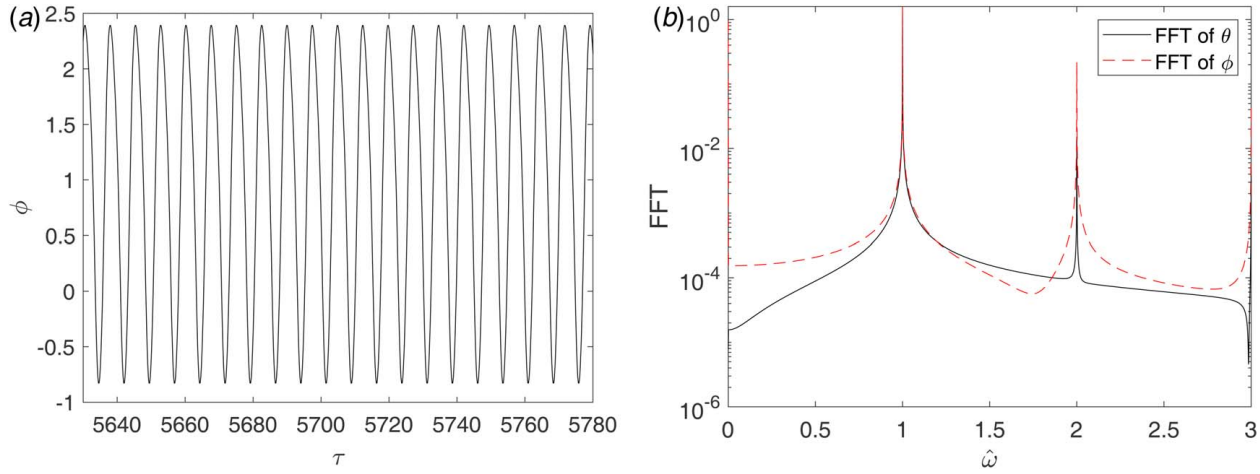

Fig. 5 (*a*) Time series and (*b*) FFT of the pendulum motion at point ×1

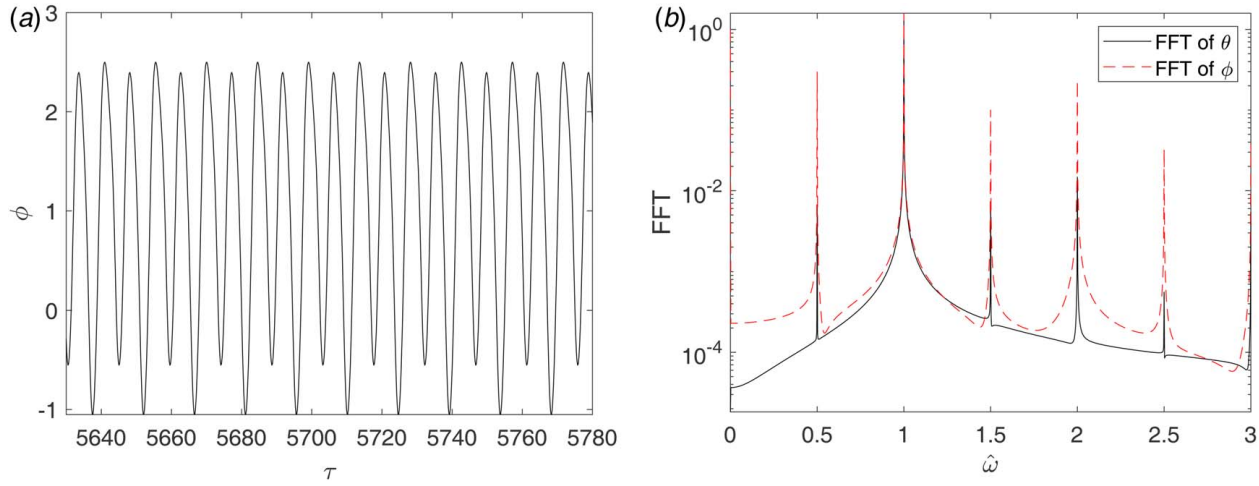

Fig. 6 (*a*) Time series and (*b*) FFT of the pendulum motion at point ×2

frequency matches the resonant frequency of the IPVA system (given by the frequency corresponding to the lowest wave height in the stability boundary; see Fig. 4). We perform direct numerical simulation for both the IPVA and the linear system using the explicit Runge–Kutta (4,5) integration method (implemented in MATLAB's ode45), with integration kernel evaluated using an impulse to state-space converter [32,38]. Fixing the wave height to 5.5 cm, we calculate the response amplitude operator (RAO) of the spar for both the IPVA and the linear system, defined by the response of the spar divided by the wave height. Figure 8(*a*) shows the comparison of the RAO between the IPVA and the linear system. The range for the secondary resonance is marked by vertical dash-dot lines. Figure 8(*b*) shows the values of motion of the ball screw ($\dot{\theta}^2$) and the pendulum ($\dot{\phi}^2$) of the IPVA system, and the motion of the ball screw ($\dot{\theta}^2$) for the linear system. In the literature, ball screw and pendulum angular motions are used to drive electrical generators for wave energy production and the electrical power is proportional to the angular velocities squared, [32,39,40], for example. Therefore, the angular velocities squared are used to examine the energy conversion potential in this work.

As can be seen in Figs. 8(*a*) and 8(*b*), the linear system sacrifices the spar's response for the resonant ball-screw angular motion. The IPVA system, on the other hand, has a significant smaller RAO in comparison with the linear system. It can be readily seen that till around the frequency 0.4 Hz, the ball-screw motion of the linear system and the IPVA system closely follow each other in amplitude. However, the solution starts to deviate around 0.4 Hz due to increase in motion of the pendulum, and soon around 0.42 Hz, in the range corresponding to the secondary solutions (marked by dash-dot lines in the figure) in the IPVA system, the energy transfer from the primary system to the pendulum begins. Hence, it is evident that the energy in the ball-screw transfers to the pendulum due to internal resonance, resulting in suppression of the spar motion and pumping of the pendulum's kinetic energy. From Fig. 8(*b*), it can be clearly seen that the motion of the linear system is better than the IPVA system if the we consider the motion of the pendulum alone for the IPVA system. However, if we use the difference between the angular motion of the pendulum and the ball screw, the motion of the IPVA system is significantly higher than the linear system. This is because it has been observed that the ball screw and the pendulum motion are generally out of phase for the IPVA system [31,32]. A mechanism that converts the difference of angular motions into one angular motion to drive a generator can be readily achieved using a planetary gear setup; see Ref. [32]. This mechanism justifies the use of the angular motion difference to examine the energy conversion potential. Note that since the pendulum is locked for the linear system, there is effectively no pendulum damping in the linear system's equation of motion. Therefore, it is worth investigating how the pendulum damping can affect the angular motions in the IPVA system (while the linear system stays the same).

To study the effect of pendulum's damping on the performance of the IPVA system, we calculate the 1:2 internal resonance or

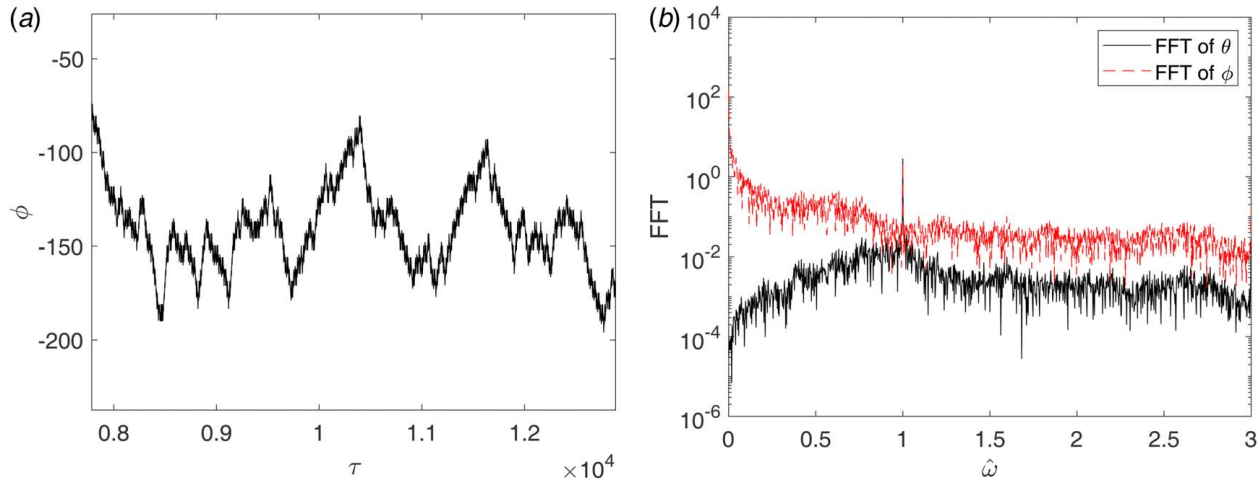

Fig. 7 (*a*) Time series and (*b*) FFT of the pendulum motion at point ×3

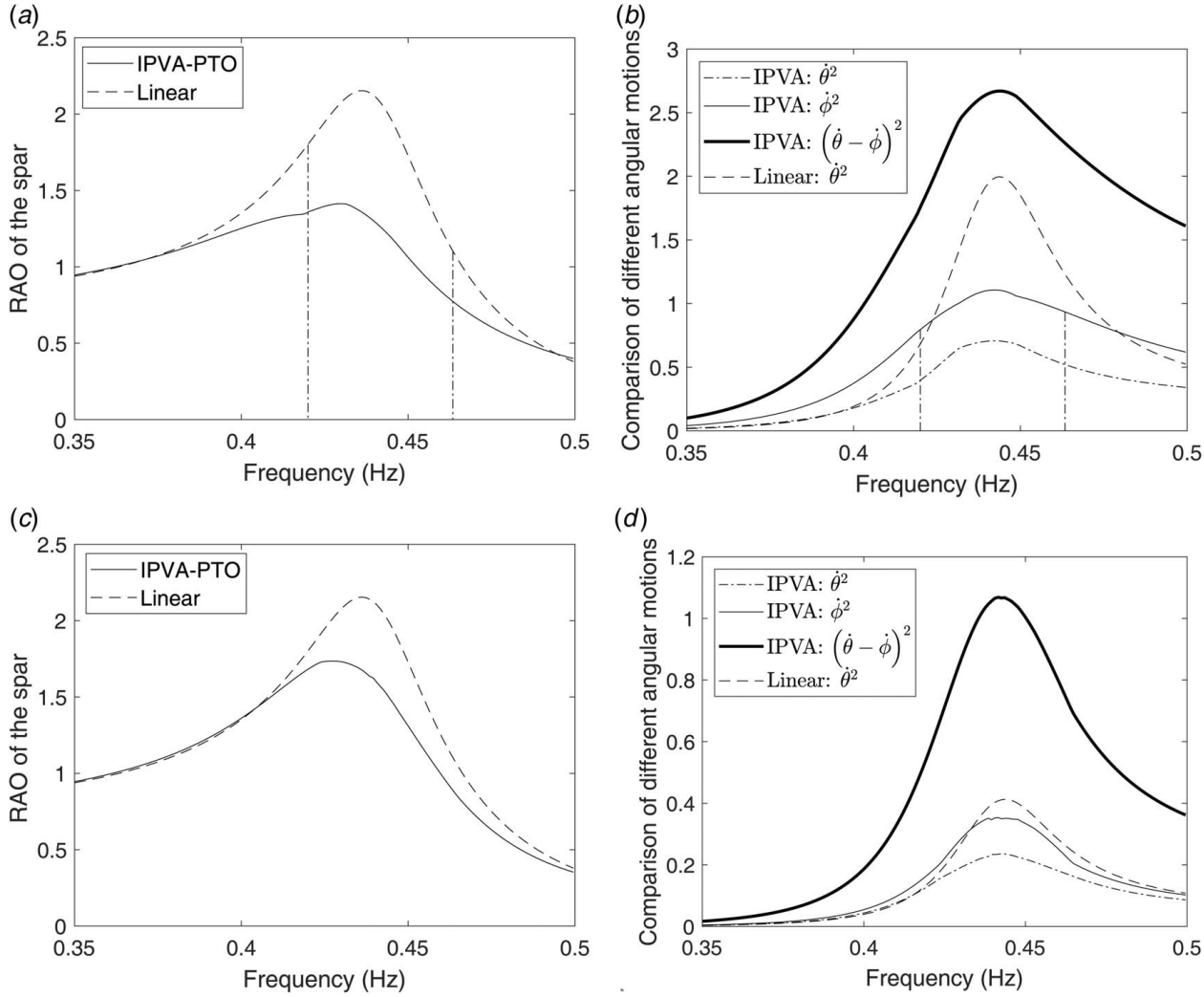

Fig. 8 The frequency responses of the linear and the IPVA system: (*a*) comparison between motion of spar for IPVA and linear system for the parameters mentioned in Fig. 4 with $\xi_p = 0.02$, (*b*) comparison of energies in the IPVA system for the parameters mentioned in Fig. 4 with $\xi_p = 0.02$, (*c*) comparison between motion of spar for IPVA and linear system for the parameters mentioned in Fig. 4 with $\xi_p = 0.01$, and (*d*) comparison of energies in the IPVA system for the parameters mentioned in Fig. 4 with $\xi_p = 0.01$

period-doubling bifurcation boundary for the IPVA system with a different damping value, taken as $\xi_p = 0.01$. This boundary is shown in Fig. 9(*d*) as a part of parametric studies (to be discussed later). It can be seen that the stability boundary for the case of $\xi_p = 0.01$ is significantly lower than $\xi_p = 0.02$ shown in Fig. 4. Therefore, we choose a wave height of 2.5 cm to perform the numerical frequency response analysis for the case of $\xi_p = 0.01$. The frequency response is shown in Figs. 8(*c*) and 8(*d*). We can observe a similar energy transfer phenomenon and vibration suppression in the spar's RAO. However in this case, motion value of the IPVA defined in terms of $\left(\dot{\theta}-\dot{\phi}\right)^2$ is around three times higher than the linear system compared to the case of $\xi_p = 0.02$, where the same motion is around 1.5 times higher. Another thing worth mentioning is that the RAO of the spar for $\xi_p = 0.01$ is higher than that of $\xi_p = 0.02$, though it still outperforms the linear system. Next, let us look at the effects of system parameters on the stability boundary.

2.5 Parametric Studies. To analyze the effects of various system parameters on the stability boundary of internal resonance (period-doubling bifurcation), we vary the following parameters μ_r, η, ξ, and ξ_p while keeping the other parameters fixed at their values mentioned in Fig. 4. First, we see the effect of μ_r on the stability boundary. Recall that μ_r is the mass amplification factor in the system given by $\mu_r = \dfrac{mR_p^2}{MR^2}$. As the μ_r value increases, we see the wave height required to cross the internal boundary decreases as evident from Fig. 9(*a*). Therefore to control the wave height required to cross the boundary, one can readily change the value of $\dfrac{R_p}{R}$, which is the ratio of the distance of the pendulum pivot point with respect to the carrier over the effective radius of the ball-screw system. Next, the effect of η, defined by $\dfrac{r}{R_p}$ where r is the length of the pendulum, on stability boundary is analyzed. As observed from Fig. 9(*b*), for larger values of η, the wave height required to cross the boundary for a given frequency decreases. Figures 9(*c*) and 9(*d*) show the effect of mechanical and pendulum damping respectively on the stability boundary. It can be observed that the wave height required to reach 1:2 internal resonance increases with increase in both the mechanical and pendulum damping value. The next section discusses the experimental verification for the IPVA system.

3 Experimental Analysis

To verify the analysis performed, experiments consisting of a "dry" IPVA (without any hydrodynamic effects on the system) integrated with a single-degree-of-freedom system are conducted. As has been demonstrated previously, the dry system also shows the internal resonance phenomenon [31], and it can be explained as

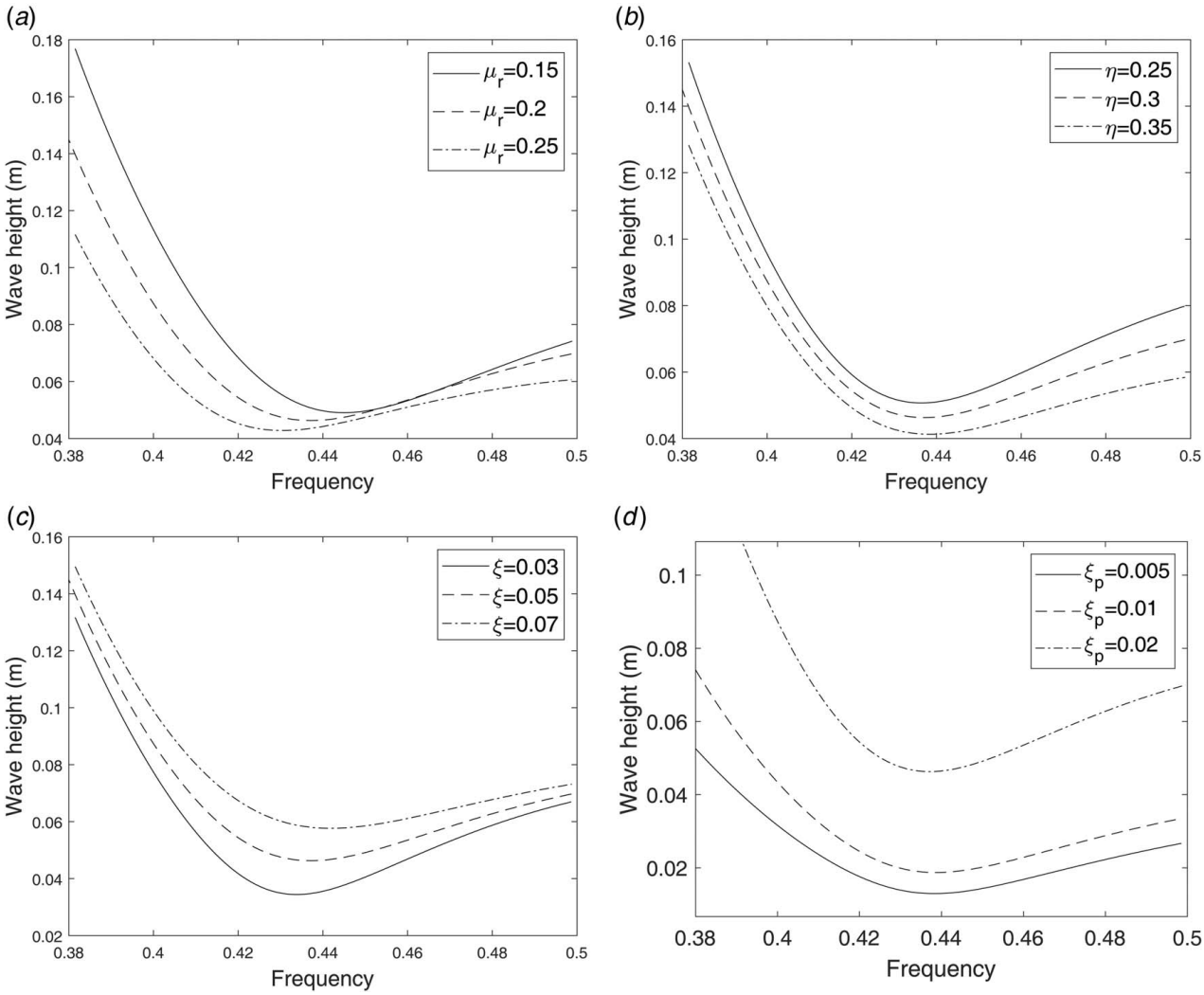

Fig. 9 Effect of various system parameters on the stability boundary, all the values are from Fig. 4 except for the parameter value specified in the figure: (*a*) stability boundaries for different values of μ_r, (*b*) stability boundaries for different values of η, (*c*) stability boundaries for different values of ξ, and (*d*) stability boundaries for different values of ξ_p

follows. The hydrodynamic effects on the system add a frequency-dependent mass, damping, and a force to the system. If we fix a frequency value—then the mass, the stiffness, and the damping matrix can be calculated at that frequency value, and a force can be obtained corresponding to the boundary point of the internal resonance boundary. This boundary can be obtained for all the frequency values as explained. Now, if the mass, stiffness, and damping matrix do not change with frequency, we can still obtain a force corresponding to internal resonance boundary at a specified frequency, and do the procedure for all the frequencies to obtain an internal resonance boundary. Thus, in principle, the internal resonance boundary for the dry system can be obtained. Although it maybe different than the system with hydrodynamic effects, the boundary will still exist. Thus, the aim of the experiments is to verify the energy transfer between the primary system and the pendulum vibration absorber and the secondary resonance phenomenon of the IPVA (harmonics of frequency $\omega/2$). An experimental setup is created by integrating a single-degree-of-freedom system with the IPVA system as shown in Fig. 10. Table 2 shows the description of labels for various components of the experimental setup. The top plate, marked by plate *A*, supports the primary mass. The base plate system contains three plates, plates *B*, *C*, and *D*. Plate *D* is directly connected to the shaker, whereas the nut of the ball-screw system connects plate attached to the plate *B*. Note that the plates *B*, *C*, and *D* are rigidly connected. A coupler connects the ball-screw system with the carrier which hosts the pendulum. The eight springs are connected between the primary mass system and the base plate system. Therefore, due to the excitation of the base plate system, the top plate system starts moving. The relative motion between the top plate and the base plate system drives the screw (as the nut is fixed to the base plate system), i.e.,

$$\theta = \frac{x - y}{R}$$

where x is the motion of plate *A* and y is the motion of plate *D*. The pendulum is free to rotate and is connected to the carrier by a ball bearing. A shaker (APS 113) excites the base plate by controlling the motion of the plate *D* and is driven by a spectral analyzer and controller (Spider 80x) using an amplifier. There is an accelerometer connected to the base plate for closed-loop control of the shaker, and an accelerometer is connected to the top plate to monitor the motion of the top plate system. An encoder is mounted on the pendulum shaft to measure the motion of the pendulum using a microcontroller (US Digital).

3.1 Equations of Motion for the Experimental Setup. The equations of motion of the experimental system can be directly derived from Eq. (9), converting the forced excitation into base

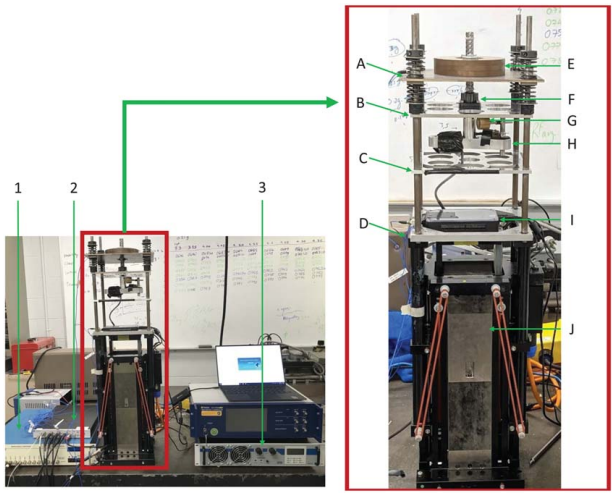

Fig. 10 Experimental setup

excitation (of the shaker) and removing the floater. To obtain this equation of motion, we assume perfect transmission by the ball-screw system. Thus, the resultant equation of motion is given by

$$\bar{\mathbf{M}}\ddot{\bar{\mathbf{x}}} + \bar{\mathbf{C}}\dot{\bar{\mathbf{x}}} + \bar{\mathbf{K}}\bar{\mathbf{x}} + \bar{\mathbf{G}}(\bar{\mathbf{x}}, \dot{\bar{\mathbf{x}}}, \ddot{\bar{\mathbf{x}}}) = \bar{\mathbf{F}} \tag{10}$$

where

$$\bar{\mathbf{M}} = \begin{bmatrix} 1+\mu_r+\mu_r\eta^2+2\eta\mu_r\cos(\phi)+\mu_{bsc}+\mu_p & \mu_p+\mu_r\eta^2+\mu_r\eta\cos(\phi) \\ \mu_p+\mu_r\eta^2+\mu_r\eta\cos(\phi) & \mu_p+\mu_r\eta^2 \end{bmatrix}$$

$$\bar{\mathbf{K}} = \begin{bmatrix} 1 & 0 \\ 0 & 0 \end{bmatrix}, \quad \bar{\mathbf{C}} = \begin{bmatrix} 2\xi & 0 \\ 0 & 2\xi_p \end{bmatrix}, \quad \bar{\mathbf{G}} = \mu_r\eta\begin{pmatrix} -2\theta'\phi'\sin(\phi) - \phi'^2\sin(\phi) \\ \theta'^2\sin(\phi) \end{pmatrix} \tag{11}$$

$$\bar{\mathbf{F}} = \begin{pmatrix} -y'' \\ -t_{fp}\,\mathrm{sign}(\dot{\phi}) \end{pmatrix}$$

with $\bar{\mathbf{x}} = [\theta, \phi]^T$ and $t_{fp} = \dfrac{T_f}{MR^2}$, where T_f is the friction between the shaft of the pendulum and its bearing. Here, x is the motion of the top plate, y is the motion of the shaker, θ is the rotation of the carrier, R_p is the location of the shaft of the pendulum with respect to the center of the ball-screw system, ξ_p is the damping coefficient of the pendulum defined by $\xi_p = \dfrac{c_p}{M\omega_0 R^2}$, c_p being the damping between the pendulum's shaft and ball bearing. M is the mass of the top plate (the primary structure), J_{bsc} includes the inertia of carrier, ball screw, coupler, and encoder and J_p is the moment of inertia of the pendulum system with respect to its center of mass. We assume theoretical values for all the inertia, masses, transmission ratio, springs, and lengths in the system. Therefore, the values of m, R_p, M, R, J_p, J_{bsc}, k, r, and ω_0 are assumed to be known; see Table 3. This leaves c and c_p to be experimentally identified, which is discussed next.

3.2 Obtaining the Mechanical Damping *c*. The mechanical damping value c is obtained by removing the pendulum from the experimental setup and obtaining its frequency response function (FRF). The measured FRF and theoretical FRF are correlated with each other to obtain the mechanical damping value. The linear system without the pendulum has the following equation of motion:

$$\hat{M}\ddot{x} + kx + c\dot{x} = M\ddot{y} + c\dot{y} + ky \tag{12}$$

where

$$\hat{M} = M(1+\mu_{bsc}), \quad \mu_{bsc} = \frac{J_{bsc}}{MR^2} \tag{13}$$

Using $x = \dfrac{X}{\omega^2}e^{i\omega t}$ and $y = \dfrac{Y}{\omega^2}e^{i\omega t}$ where X and Y denote the displacement amplitude of the base plate and the top plate respectively, and defining $r = \dfrac{\omega}{\omega_0}$, we obtain

$$\frac{X}{Y} = \frac{\mu_{bsc}^2 r^4 - 2\mu_{bsc}r^2 + 4\xi^2 r^2 + 1}{(\mu_{bsc}+1)^2 r^4 - 2r^2(\mu_{bsc} - 2\xi^2 + 1) + 1} \tag{14}$$

MATLAB's "fit" function is used to fit the data and obtain the value of μ_{bsc}, ω_0, and c. We found that the value of μ_{bsc} and ω_0 were close to the theoretical values, and therefore theoretical values of μ_{bsc} and ω_0 are chosen for the analysis of experiments.

3.3 Obtaining the Pendulum Damping c_p. To obtain the pendulum damping, the pendulum and carrier were removed from the

Table 2 Labels depicting the different parts of the experimental setup

Label	Description
1	Accelerometer signal conditioner
2	Spectral analyzer and controller
3	Shaker signal amplifier
A	Top plate
B	Ball-screw mounting plate
C	Middle plate
D	Lower plate
E	Top added mass
F	Ball-screw system
G	Pendulum
H	Carrier
I	Encoder data acquisition box
J	Shaker

Table 3 Experimental parameters for the IPVA system

Parameter	Value
ξ_p	0.00418
ξ	0.242
μ_r	4.072
η	0.371
ω_0	96.98 rad/s
η_g	0.0029
T_f	0.0014 N
μ_p	0.388
μ_{bsc}	8.294

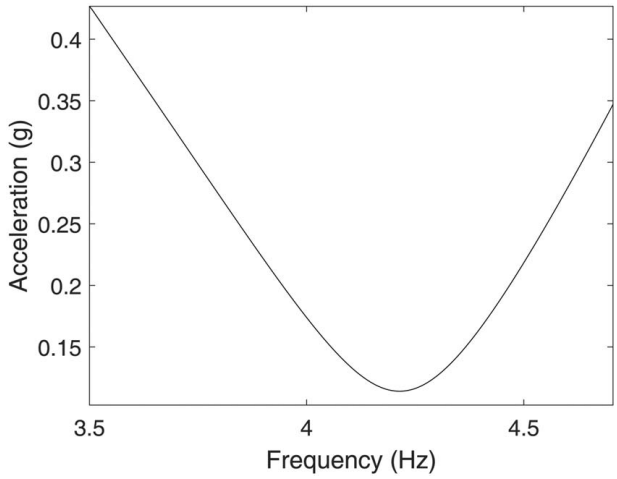

Fig. 11 Stability boundary of energy transfer corresponding to the experimental setup

ball-screw system and fixed it rigidly to the ground. The pendulum was given some initial rotational velocity and the free rotational behavior of the pendulum was observed as it came to a stop. It was observed that damping alone is insufficient to capture the effects of the energy dissipation in the pendulum, so a friction term was considered in the analysis of the interaction between the shaft of the pendulum and its bearing. The rotation of the pendulum can be modeled using the following equation of motion:

$$\left(J_p + mr^2\right)\ddot{\phi} + c_p\dot{\phi} + T_f = 0 \tag{15}$$

This Eq. (15) is integrated with respect to time to obtain

$$\left(J_p + mr^2\right)\left(\dot{\phi}_f - \dot{\phi}_i\right) + c_p\left(\phi_f - \phi_i\right) + T_f\Delta t = 0 \tag{16}$$

where Δt is the time it took for pendulum to stop, subscripts i and f on ϕ and $\dot{\phi}$ denote the initial and final values of ϕ and $\dot{\phi}$ respectively. Clearly, $\dot{\phi}_f = 0$ as the pendulum comes to a full stop. The equation can be solved to obtain c_p. The experimental parameters are tabulated in Table 3 for ready reference.

3.4 Experimental Verification. In this section, the simulation model is verified with the experiments. First, the stability boundary is obtained and shown in Fig. 11 using the theoretical and fitted parameters shown in Table 3. Since it is known that there should be vibration suppression above the stability boundary, an acceleration value of 0.2 g is used to run the experiments, which is well above the stability boundary for a range of frequencies. Before observing the experimental results and comparing them to the linear system, a few points need to be stated:

(1) The ball-screw system is assumed to be 100% efficient, with no loss in transmission;
(2) The effects of accelerometer cables on the system are neglected, and the encoder cable is assumed to only contribute to mechanical damping and moment of inertia of the ball-screw system;
(3) The springs are modeled to be linear for the analytical analysis.

3.5 Verification of the Internal Resonance. Previously, it was defined that the secondary solutions are those solutions which contain harmonics of frequency $\frac{\omega}{2}$ when the excitation frequency is ω. As has been reported in Ref. [31], internal resonance is required for the energy transfer to occur between the primary system and the pendulum vibration absorber and thus suppressing the vibrations of the primary system. To observe the secondary resonance of the system, experiments are performed on the IPVA system by fixing a frequency and increasing base acceleration value such that the secondary resonance is found. For this particular case, an excitation acceleration amplitude of 0.2 g and an excitation frequency of 4.16 Hz led to the secondary resonance, which means that the response of the system at this excitation frequency and acceleration amplitude will have harmonics of frequency half the excitation frequency (2.08 Hz), along with the excitation frequency (4.16 Hz). As can be seen from Fig. 12(*a*), the motion of the pendulum measured by the encoder shows harmonics of frequency $\frac{\omega}{2}$ ($\approx$ 2.08 Hz) as evident from the time series of the pendulum's motion and the FFT shown in Fig. 12(*b*). Moreover, it can be observed that harmonics of frequency $\frac{3\omega}{2}$ and 2ω also show up in the motion of the pendulum.

3.6 Comparison With the Linear System. Next, the IPVA system is compared with the linear system to benchmark its vibration suppression capabilities. For this, the base excitation acceleration is fixed at 0.2 g. The linear system is chosen by fixing the system's pendulum at an angle such that the natural frequency of the linear system is equal to the resonant frequency of the IPVA system. Ten frequency points are chosen for which the experiments are run on the IPVA system to get the root-mean-squared (RMS)

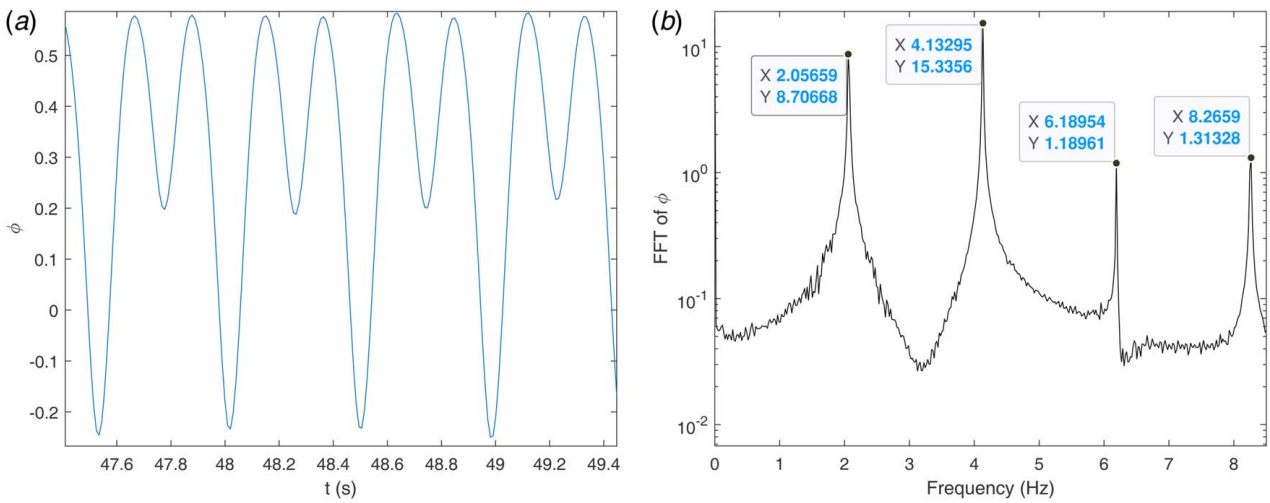

Fig. 12 (*a*) Time series and (*b*) measured FFT of the pendulum motion

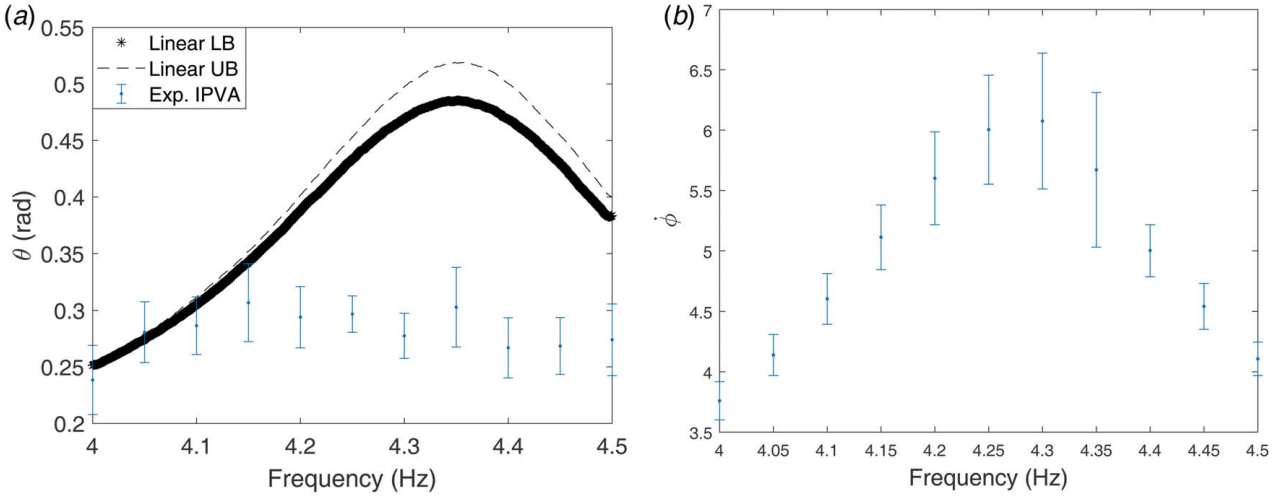

Fig. 13 Frequency response of θ and ϕ for the IPVA and the linear system (where applicable) at 0.2 g base excitation acceleration: (*a*) comparison between experimental θ RMS value for linear and the IPVA system and (*b*) experimental frequency response RMS of the pendulum for the IPVA system

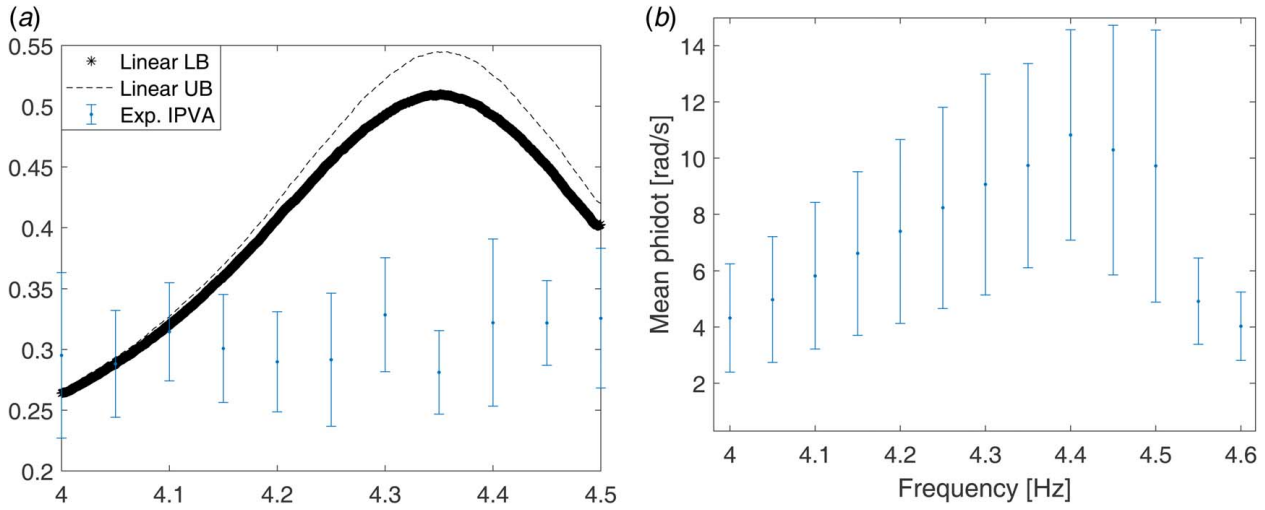

Fig. 14 Frequency response of θ and ϕ for the IPVA and the linear system (where applicable) at 0.21 g base excitation acceleration: (*a*) comparison between experimental θ RMS value for linear and the IPVA system and (*b*) experimental frequency response RMS of the pendulum for the IPVA system

values of the amplitude of ball-screw rotation (θ) and pendulum's motion (ϕ), and obtain the mean and standard deviations for both the rotations. Similar experiments are performed for the linear system by converting the frequency response function between the acceleration of the top plate A and the input base acceleration from the shaker's to RMS data for θ for the same ten frequencies as the IPVA system. Sixteen frequency response function were experimentally calculated to obtain these RMS θ values for the linear system. These RMS values are plotted against each other for comparison in Fig. 13(*a*). The "Linear LB" and "Linear UB" labels show lower bound and the upper bound of the RMS values of θ for the linear system as calculated from the frequency response function, and error bars are plotted for the ball-screw motion (θ) for the IPVA system. Figure 13(*b*) shows the motion of the pendulum observed experimentally. It is clear that the RMS values for θ do not follow a resonance-like behavior for the range of frequencies show, whereas the linear system does. This verifies that there is nonlinear energy transfer between the ball screw (the primary mass motion), and the pendulum as cross-verified from the energy pumping in the pendulum, see Fig. 13(*b*). Next, the case when the base excitation acceleration is 0.21 g is taken. As shown in Figs. 14(*a*) and 14(*b*), we see results similar to that of 0.2 g base acceleration. However, the pendulum has more energy in this case compared to 0.2 g excitation due to a saturation-like phenomenon, where the motion of the primary system (θ) does not increase significantly even though the excitation acceleration is increased. This has also been observed in a numerical study by the authors [31].

4 Conclusion

This study analyzes the incorporation of the IPVA system [31] into a heaving spar-floater system to study the energy transfer between the spar-floater system and the pendulum vibration absorber. The hydrodynamic response and wave energy conversion potential of the integrated system when the wave frequency is near the spar resonance frequency are investigated using numerical frequency response simulations. A harmonic balance method is used to determine the boundary of period-doubling bifurcation in the parameter plane of wave height and wave frequency. According to the boundary, one can determine a combination of the wave height and frequency such that 1:2 internal resonance occurs to

the IPVA system. It is observed that this 1:2 internal resonance is associated with a nonlinear energy transfer phenomenon similar to that observed in Refs. [31,32]. It is also shown that because of this energy transfer phenomenon, the IPVA-PTO system achieves a lower maximum RAO, and a higher energy transfer potential compared to the linear benchmark, when the relative angular motion between the ball-screw and the pendulum is used as a measure of energy conversion potential. The effect of the pendulum damping is also characterized in the IPVA system, since it is the only parameter which is missing from the linear benchmark. It is found that for lower pendulum damping, a lower wave height is required to achieve the energy transfer phenomenon and the angular motions of the IPVA system are significantly higher than the linear system, although the RAO value also increases compared to the higher pendulum damping case. Parametric studies showing the effects of various system parameters on the 1:2 internal resonance boundary were also shown in this study. Finally, experiments integrating the IPVA system with a single-degree-of-freedom spring mass system were performed. The secondary resonance which corresponds to the crossing of 1:2 internal resonance boundary was experimentally shown in the IPVA system. Furthermore, it was observed for two different acceleration values, that above the period-doubling bifurcation boundary (1:2 internal resonance boundary), the motion of the primary system was suppressed, and its energy transferred to the pendulum vibration absorber.

Acknowledgment

The authors would like to thank Mr. Max Wiedemann for helping in setting up the experiment. This material is based upon work supported by the start-up funding in Michigan State University and by the National Science Foundation under Grant No. 2127495. Any opinions, findings, and conclusions or recommendations expressed in this material are those of the authors and do not necessarily reflect the views of Michigan State University and the National Science Foundation.

Conflict of Interest

There are no conflicts of interest.

Data Availability Statement

The datasets generated and supporting the findings of this article are obtainable from the corresponding author upon reasonable request.

References

[1] Falcão, A. F. D. O., 2010, "Wave Energy Utilization: A Review of the Technologies," Renewable Sustainable Energy Rev., **14**(3), pp. 899–918.
[2] Gunn, K., and Stock-Williams, C., 2012, "Quantifying the Global Wave Power Resource," Renew. Energy, **44**, pp. 296–304.
[3] Baca, E., Philip, R. T., Greene, D., and Battey, H., 2022, "Expert Elicitation for Wave Energy lcoe Futures," Technical Report, National Renewable Energy Laboratory (NREL), Golden, CO.
[4] Association, U. E. I., 2022, "Levelized Costs of New Generation Resources in the Annual Energy Outlook 2022," US Department of Energy, March.
[5] Bedard, R., Hagerman, G., Previsic, M., Siddiqui, O., Thresher, R., and Ram, B., 2005, "Final Summary Report, Project Definition Study, Offshore Wave Power Feasibility Demonstration Project," Electric Power Research Institute Inc., Palo Alto, CA.
[6] Nguyen, H., Wang, C., Tay, Z., and Luong, V., 2020, "Wave Energy Converter and Large Floating Platform Integration: A Review," Ocean Eng., **213**, p. 107768.
[7] Today, O. E., 2019, "Eni's New Wave Power Device to Convert Mature Offshore Platforms Into Renewable Energy Hubs," Accessed January 31, 2021.
[8] Oliveira-Pinto, S., Rosa-Santos, P., and Taveira-Pinto, F., 2019, "Electricity Supply to Offshore Oil and Gas Platforms From Renewable Ocean Wave Energy: Overview and Case Study Analysis," Energy Convers. Manage., **186**, pp. 556–569.
[9] Bull, A. S., and Love, M. S., 2019, "Worldwide Oil and Gas Platform Decommissioning: A Review of Practices and Reefing Options," Ocean Coastal Manag., **168**, pp. 274–306.
[10] Jonkman, J., Butterfield, S., Musial, W., and Scott, G., 2009, "Definition of a 5-MW Reference Wind Turbine for Offshore System Development," Technical Report, National Renewable Energy Laboratory (NREL), Golden, CO.
[11] Bureau of Safety and Environmental Enforcement, 2021, "Platform Structures Online Query," Accessed February 1, 2021.
[12] Muliawan, M. J., Karimirad, M., and Moan, T., 2013, "Dynamic Response and Power Performance of a Combined Spar-Type Floating Wind Turbine and Coaxial Floating Wave Energy Converter," Renew. Energy, **50**, pp. 47–57.
[13] Karimirad, M., and Koushan, K., 2016, "Windwec: Combining Wind and Wave Energy Inspired by Hywind and Wavestar," 2016 IEEE International Conference on Renewable Energy Research and Applications (ICRERA), Birmingham, UK, Nov. 20–23, IEEE, pp. 96–101.
[14] Cheng, Z., Wen, T. R., Ong, M. C., and Wang, K., 2019, "Power Performance and Dynamic Responses of a Combined Floating Vertical Axis Wind Turbine and Wave Energy Converter Concept," Energy, **171**, pp. 190–204.
[15] Michailides, C., 2021, "Hydrodynamic Response and Produced Power of a Combined Structure Consisting of a Spar and Heaving Type Wave Energy Converters," Energies, **14**(1), p. 225.
[16] Babarit, A., 2015, "A Database of Capture Width Ratio of Wave Energy Converters," Renew. Energy, **80**, pp. 610–628.
[17] Wan, L., Gao, Z., and Moan, T., 2015, "Experimental and Numerical Study of Hydrodynamic Responses of a Combined Wind and Wave Energy Converter Concept in Survival Modes," Coastal Eng., **104**, pp. 151–169.
[18] Suzuki, H., and Sato, A., 2007, "Load on Turbine Blade Induced by Motion of Floating Platform and Design Requirement for the Platform," ASME 2007 26th International Conference on Offshore Mechanics and Arctic Engineering, San Diego, CA, June 10–15, Vol. 42711, pp. 519–525.
[19] Yue, M., Liu, Q., Li, C., Ding, Q., Cheng, S., and Zhu, H., 2020, "Effects of Heave Plate on Dynamic Response of Floating Wind Turbine Spar Platform Under the Coupling Effect of Wind and Wave," Ocean Eng., **201**, p. 107103.
[20] Koo, B., Kim, M., and Randall, R., 2004, "Mathieu Instability of a Spar Platform With Mooring and Risers," Ocean Eng., **31**(17–18), pp. 2175–2208.
[21] Subbulakshmi, A., and Sundaravadivelu, R., 2016, "Heave Damping of Spar Platform for Offshore Wind Turbine With Heave Plate," Ocean Eng., **121**, pp. 24–36.
[22] Liang, C., 2016, "On the Dynamics and Design of a Wave Energy Converter With Mechanical Motion Rectifier," Ph.D. thesis, State University of New York at Stony Brook, Stony Brook, NY.
[23] Babarit, A., Hals, J., Muliawan, M. J., Kurniawan, A., Moan, T., and Krokstad, J., 2012, "Numerical Benchmarking Study of a Selection of Wave Energy Converters," Renew. Energy, **41**, pp. 44–63.
[24] Meng, F., Sergiienko, N., Ding, B., Zhou, B., Da Silva, L. S. P., Cazzolato, B., and Li, Y., 2023, "Co-Located Offshore Wind-Wave Energy Systems: Can Motion Suppression and Reliable Power Generation Be Achieved Simultaneously," Appl. Energy, **331**, p. 120373.
[25] Yan, Z., and Hajj, M. R., 2015, "Energy Harvesting From an Autoparametric Vibration Absorber," Smart Mater. Struct., **24**(11), p. 115012.
[26] Yan, Z., and Hajj, M. R., 2017, "Nonlinear Performances of an Autoparametric Vibration-Based Piezoelastic Energy Harvester," J. Intell. Material Syst. Struct., **28**(2), pp. 254–271.
[27] Kecik, K., 2018, "Assessment of Energy Harvesting and Vibration Mitigation of a Pendulum Dynamic Absorber," Mech. Syst. Signal Process., **106**, pp. 198–209.
[28] Felix, J. L. P., Balthazar, J. M., Rocha, R. T., Tusset, A. M., and Janzen, F. C., 2018, "On Vibration Mitigation and Energy Harvesting of a Non-Ideal System With Autoparametric Vibration Absorber System," Meccanica, **53**(13), pp. 3177–3188.
[29] Hatwal, H., Mallik, A., and Ghosh, A., 1983, "Forced Nonlinear Oscillations of an Autoparametric System–Part 1: Periodic Responses."
[30] Vyas, A., and Bajaj, A., 2001, "Dynamics of Autoparametric Vibration Absorbers Using Multiple Pendulums," J. Sound. Vib., **246**(1), pp. 115–135.
[31] Gupta, A., and Tai, W.-C., 2022, "The Response of an Inerter-Based Dynamic Vibration Absorber With a Parametrically Excited Centrifugal Pendulum," ASME J. Vib. Acoust., **144**(4), p. 041011.
[32] Gupta, A., and Tai, W.-C., 2022, "Ocean Wave Energy Conversion of a Spar Platform Using a Nonlinear Inerter Pendulum Vibration Absorber," International Design Engineering Technical Conferences and Computers and Information in Engineering Conference, Vol. 86311, American Society of Mechanical Engineers, p. V010T10A013.
[33] Mérigaud, A., 2018, "A Harmonic Balance Framework for The Numerical Simulation of Non-Linear Wave Energy Converter Models in Random Seas," Ph.D. thesis, National University of Ireland, Maynooth, Ireland.
[34] Cummins, W., Iiuhl, W., and Uinm, A., 1962, "The Impulse Response Function and Ship Motions."
[35] Ogilvie, T. F., 1964, "Recent Progress Toward the Understanding and Prediction of Ship Motions," 5th ONSymposium on Naval Hydrodynamics, Bergen, Norway, Sept. 10–12.
[36] Beatty, S. J., Hall, M., Buckham, B. J., Wild, P., and Bocking, B., 2015, "Experimental and Numerical Comparisons of Self-Reacting Point Absorber Wave Energy Converters in Regular Waves," Ocean Eng., **104**, pp. 370–386.
[37] Seebai, T., and Sundaravadivelu, R., 2011, "Dynamic Analysis of Slack Moored Spar Platform With 5 MW Wind Turbine," Ocean Syst. Eng., **1**(4), pp. 285–296.
[38] Kristiansen, E., Hjulstad, Å., and Egeland, O., 2005, "State-Space Representation of Radiation Forces in Time-Domain Vessel Models," Ocean Eng., **32**(17–18), pp. 2195–2216.
[39] Li, X., Chen, C., Li, Q., Xu, L., Liang, C., Ngo, K., Parker, R. G., and Zuo, L., 2020, "A Compact Mechanical Power Take-Off for Wave Energy Converters: Design, Analysis, and Test Verification," Appl. Energy, **278**, p. 115459.
[40] Yurchenko, D., and Alevras, P., 2018, "Parametric Pendulum Based Wave Energy Converter," Mech. Syst. Signal Process., **99**, pp. 504–515.